

Journal of MARINE RESEARCH

Volume 68, Number 2

Water-mass transformation in the shelf seas

by Gualtiero Badin^{1,2}, Richard G. Williams^{1,3} and Jonathan Sharples^{1,4}

ABSTRACT

The rate at which water masses are transformed from one density class to another is assessed in the shelf seas using the Walin (1982) framework. For a tidal-mixing front, the transformation is estimated using air-sea density fluxes and the diapycnal mixing diagnosed from a series of one-dimensional mixed layer models running across the shelf. These transformation rates diagnosed from the air-sea fluxes and diapycnal mixing agree with volume changes diagnosed directly from the model. The transformation from air-sea fluxes reaches a maximum amplitude typically twice that provided by diffusive mixing. This framework is extended to estimate the rate at which nutrients are converted in nutrient space including the effects of biological consumption. The transformation in density and nutrient space are broadly related in the spring when there is a relatively tight relationship between density and nutrient concentrations. For a shelf-break front in the Celtic Seas, the transformation is estimated from a combination of observed air-sea fluxes, remotely-sensed sea surface temperature and ship-based measurements of density and turbulent mixing. The transformation is controlled by diapycnal mixing along dense surfaces and by air-sea fluxes for lighter surfaces, and each contribution reaches comparable magnitudes over a six-month period.

1. Introduction

Walin (1982) provided an elegant theory of how water masses are transformed from one density class to another through the action of air-sea fluxes and turbulent mixing. This framework has been employed in the open ocean to exploit the patterns of air-sea fluxes and predict the rates of mode water formation (Speer and Tziperman, 1992; Speer *et al.*, 1995) and link to the ventilation rates from the winter mixed layer (Marshall *et al.*, 1999),

1. School of Environmental Sciences, University of Liverpool, Liverpool, L69 3GP, United Kingdom.
2. Present address: Department of Earth Sciences, Boston University, Boston, Massachusetts, 02215, U.S.A.
3. Corresponding author: *email: ric@liverpool.ac.uk*
4. National Oceanography Centre, Liverpool, L3 5DA, Liverpool, United Kingdom.

as well as connect to the residual circulation in the Southern Ocean (Marshall, 1997; Badin and Williams, 2010).

A potential difficulty though is the poor knowledge of diapycnal mixing. For a steady state over a closed domain, the rates at which water masses form from air-sea fluxes has to be balanced by the effect of diapycnal mixing. The skill of open ocean predictions, made only through knowledge of the air-sea fluxes, relies on the separation of the sites of water-mass formation from the regions of strong diapycnal mixing. In a model assessment for the North Atlantic, mode waters were formed at mid and high latitudes through the action of air-sea fluxes, while strong diapycnal mixing was instead concentrated within the upper thermocline in the tropics (Nurser *et al.*, 1999). Speer (1997) exploited this separation to diagnose the integrated rates of diapycnal mixing based upon volume fluxes across a zonal section and water-mass formation rates from air-sea fluxes.

In this study, we consider the shelf seas, a challenging region where both air-sea fluxes and diapycnal mixing sustained by strong tidal flows are important. A tidal-mixing front separates contrasting regions of well-mixed and stratified waters in summer, while a shelf-break front separates the shelf waters from the open ocean. For example, in the northwest European shelf, there are well mixed waters in the Irish Sea and stratified waters in the Celtic Sea (Fig. 1a,b), where as one moves onshore, surface waters cool, the thermocline thins and the bottom mixed layer thickens. Associated with this physical structure, there is a subsurface chlorophyll maximum running along the thermocline and generally enhanced chlorophyll concentration in the well mixed waters (Fig. 1c,d).

Our aim is to apply the Walin framework to the shelf seas, which has previously been exploited for a freshwater budget study of an estuary in salinity space (MacCready and Geyer, 2001; MacCready *et al.*, 2002). In our study, firstly we consider the seasonal migration of the tidal-mixing front in terms of the transformation of water masses, examining the relative importance of the air-sea forcing and tidal mixing. Secondly, we consider how much water mass is transformed across the shelf-break front, connecting the open ocean and shelf sea.

The paper is structured in the following manner: the Walin framwork is presented in Section 2, setting out how the transformation and formation rates are obtained. The water-mass transformation in density space across the tidal-mixing front in the shelf seas is then diagnosed in Section 3 using a series of one-dimensional mixed-layer models. The Walin framework is then applied in nutrient space in Section 4, diagnosing how water-masses are converted from one nutrient class to another. The implications of the Walin framework are then assessed for the shelf-break front in the Celtic Sea in Section 5, using a range of data sources. Finally, the implications of this framework for the shelf seas is summarized in Section 6.

2. Water-mass transformation and formation for a tidal-mixing front

Following Walin (1982) and Nurser *et al.* (1999), consider a volume of fluid, ΔV , bound by the ρ and $\rho + \Delta\rho$ isopycnals, with an upper boundary given by the sea surface and an open boundary where the volume is connected to the rest of the ocean interior (Fig. 2a).

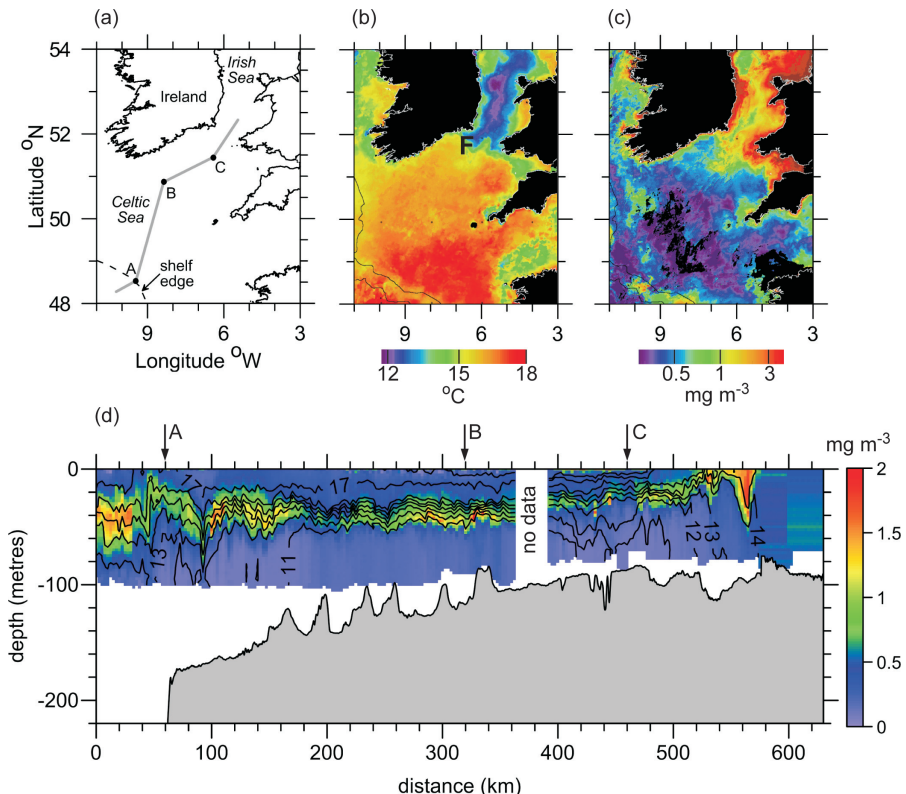


Figure 1. (a,d) Summer section of temperature ($^{\circ}\text{C}$) and chlorophyll (mg Chl m^{-3} , colors) in the European Shelf passing from well mixed waters ((d) right) in the Irish Sea to the shelf edge ((d) left), from cruise JR98, RRS *James Clark Ross*, July 2003; (b) and (c), remotely-sensed measurements of surface temperature ((b), $^{\circ}\text{C}$) and chlorophyll ((c), mg Chl m^{-3}); chlorophyll *a* concentration (b,d) show biological activity along the pycnocline with enhanced activity at the tidal front and at the shelf break front.

The volume budget is defined by a balance between the temporal increase in the volume element, ΔV , the volume flux out of the domain through the open boundary, $\Delta\Psi$, the volume influx into the domain from surface freshwater input, $\Delta\Psi_{P-E}$, and the difference in the diapycnal volume fluxes passing into the layer, $G(\rho)$, and out of the layer $G(\rho + \Delta\rho)$,

$$\left(\frac{\partial \Delta V}{\partial t} + \Delta\Psi - \Delta\Psi_{P-E} \right) = G(\rho) - G(\rho + \Delta\rho) = -\Delta\rho \frac{\partial G}{\partial \rho} \equiv M\Delta\rho, \quad (1)$$

where the volume fluxes, G and $\Delta\Psi$, have units of $\text{m}^3 \text{s}^{-1}$. The rate of accumulation of water between two isopycnals ρ and $\rho + \Delta\rho$ is referred to as the water-mass formation rate, $M\Delta\rho$, defined by the left-hand side of (1).

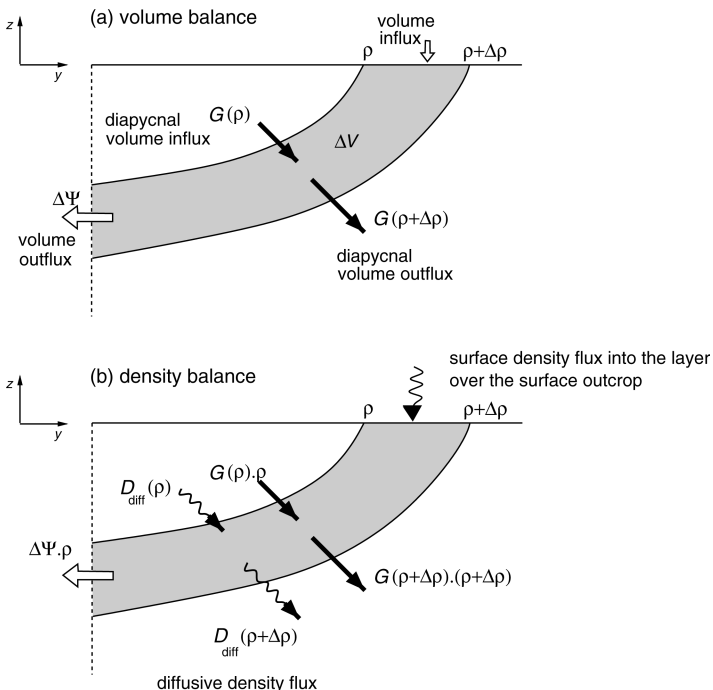


Figure 2. Schematic vertical sections showing (a) volume and (b) the density budgets for a volume element bounded by the density surfaces ρ and $\rho + \Delta\rho$ that outcrop at the sea surface. The volume balance depends on the diapycnal volume fluxes, G , the volume outflux $\Delta\Psi$, and the volume influx over the surface outcrop from freshwater fluxes. The density content of the layer depends on the advective change from the diapycnal volume flux, ρG , the mass exiting the domain, $\rho \Delta\Psi$, as well as the density gained from the atmosphere from the surface density flux over the surface outcrop, $\int_{\text{outcrop}} \mathcal{D}_{\text{in}} dA$ and the difference in the diffusive density fluxes across the layer, D_{diff} . Modified from Nurser *et al.* (1999).

The density budget of the control volume between the ρ and $\rho + \Delta\rho$ isopycnals is given by a balance between advective and diffusive density fluxes through the bounding isopycnals, ρ and $\rho + \Delta\rho$, and the outcrop of the layer at the sea surface (Fig. 2b),

$$\left(\frac{\partial \Delta V}{\partial t} + \Delta\Psi - \Delta\Psi_{P-E} \right) \rho + \Delta\rho \frac{\partial}{\partial \rho} (\rho G) = -\Delta\rho \frac{\partial D_{\text{diff}}}{\partial \rho} + \int_{\text{outcrop}} \mathcal{D}_{\text{in}} dA, \quad (2)$$

where the surface density flux is given by $\mathcal{D}_{\text{in}} = -\frac{\alpha T}{C_p} \mathcal{H} + \rho \beta_S S(\mathcal{E} - \mathcal{P})$ and has units of mass per unit area and unit time, $\text{kg m}^{-2} \text{s}^{-1}$; the surface heat flux, $\mathcal{H}(x, y)$, is positive when directed into the ocean and $\mathcal{E}(x, y)$ and $\mathcal{P}(x, y)$ are, respectively, the evaporation and precipitation rates, $C_p(T)$ is the heat capacity for sea water at constant pressure, $\alpha(T)$ and $\beta(T)$ are, respectively, the temperature dependent thermal expansion and the haline contraction coefficients of sea-water, $S(x, y)$ is the salinity and ρ_0 is a reference density.

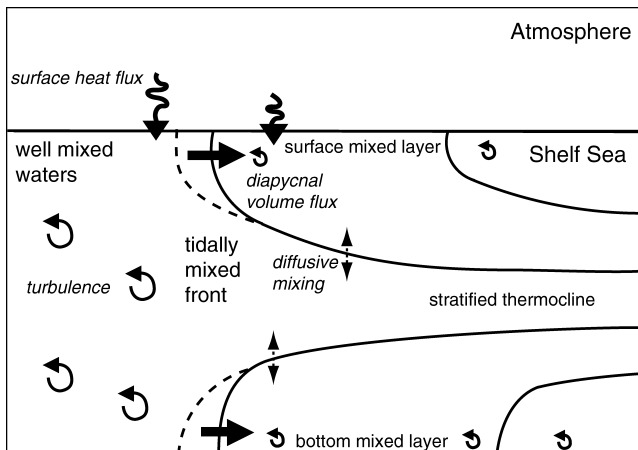


Figure 3. A schematic of a tidal-mixing front separating well mixed and stratified waters. The position of the front is controlled by a competition of surface buoyancy forcing and mechanical mixing from tides and winds. If there is a surface heat and buoyancy input, the front migrates onshore leading to denser well-mixed waters being converted to lighter, surface waters; diapycnal volume flux indicated by horizontal arrows, turbulence by circular arrows, diffusive mixing by double arrows, isopycnals by full lines and new position of isopycnals after surface heating by dashed lines.

Combining the volume and density budgets, (1) and (2), and dividing by $\Delta\rho$, gives a diagnostic relationship for the diapycnal volume flux, $G(\rho)$, which is also referred to as the transformation rate,

$$G = -\frac{\partial D_{diff}}{\partial \rho} + \frac{1}{\Delta\rho} \int_{outcrop} \mathcal{D}_{in} dA. \quad (3)$$

A diapycnal volume flux directed from light to dense water, $G(\rho) > 0$, requires a density supply either from the surface input of density, $\int_{outcrop} \mathcal{D}_{in} dA > 0$, or from a convergence of diffusive density fluxes, $-\partial D_{diff}/\partial \rho > 0$. Following the right-hand side of (1), this diapycnal volume flux then creates a formation of water in a denser class (where there is convergence) and a loss of water in a lighter class (where there is divergence).

In physically interpreting the diapycnal volume flux, there are two limits: the volume flux across the density surface can either be created through (i) a physical movement of the water across stationary density surfaces or (ii) through a migration of the density surfaces without a movement of fluid particles.

In the following sections, two cases are considered: the transformation of water masses associated with the migrating tidal-mixing front and the stationary shelf-break front, located by the topographic slope (Fig. 1a,b). For the tidal-mixing front, the transformation is primarily achieved by the migration of the isopycnals (Fig. 3, dashed lines), while the transformation across the shelf-break front is associated with both an actual movement of water and a migration of isopycnals.

3. Model assessment for a tidal-mixing front

The Walin framework is now applied to the tidal-mixing front, where there is a competition between surface buoyancy input acting to stratify surface waters opposed by mechanical forcing from the tides and winds acting to mix the water column (Simpson and James, 1986; Simpson, 1988). The tidal-mixing front marks the transition between the open ocean and coast during summer where the mechanical forcing becomes sufficiently strong to mix the entire water column. This front migrates with the seasonal variation in the surface buoyancy forcing, as well as oscillates with the spring-neap cycle as the tidal forcing waxes and wanes.

a. Model formulation

The physical structure of the shelf seas is primarily controlled by a dominance of vertical processes over horizontal exchange (Simpson and Sharples, 1994). Consequently, a series of one-dimensional, mixed-layer models are used to synthesize a section passing through a tidal mixing front (Sharples *et al.*, 2006; Sharples, 2008). At each horizontal position, the model solves for the density structure based upon the surface density fluxes and mechanical forcing from the tides and winds. Vertical turbulent mixing is described using the $k-\epsilon$ turbulence scheme of Canuto *et al.* (2001). For simplicity, the contributions of the freshwater fluxes to the density fluxes have not been included within the model, although the diagnostic framework can automatically include them. The air-sea heat flux is solved through bulk aerodynamic formulas, depending on the difference in air temperature and sea-surface temperature (Gill, 1982). The suite of mixed-layer models is integrated over a repeating year, so that the modeled section is close to a steady state.

The role of advection in controlling these frontal positions has been shown to be negligible, with theory that does not incorporate the usually weak mean flows successfully predicting the positions of the fronts (Simpson, 1981). Our one-dimensional approach to modeling tidal mixing fronts has previously been used to simulate both the position of the fronts and their adjustment over the spring-neap tidal cycle in agreement with observations and theoretical predictions (Simpson and Sharples, 1994; Sharples, 2008).

The model also incorporates a simple biogeochemical component, simulating the response of phytoplankton to changes in dissolved inorganic nitrogen and light within the seasonally and tidally varying physical environment (Sharples, 2008). The tidal mixing front under consideration is assumed to be well away from riverine advective sources of nutrients and any nutrient supplies from the shelf edge, as is the case for most tidal mixing fronts on the NW European shelf. The very weak mean flows across the fronts suggest a negligible role for local nutrient advection, supporting the dominant role of local recycling and vertical mixing at least on the seasonal-annual time scales under consideration here. Even at fronts, the horizontal contrasts in vertical mixing turn out to dominate the nutrient supply sustaining primary production at the front (Loder and Platt, 1985), although there might be weaker contributions from the cross-frontal transfers by baroclinic eddies (Badin *et al.*, 2009).

b. Physical structure

The model reproduces the expected seasonal cycle in stratification over the shelf seas: well-mixed waters over much of the shelf in winter, then changing in summer to well mixed waters close to the coast and stratified waters farther offshore. At the peak of warming during summer, there are well-mixed waters confined close to the shore and lighter waters farther offshore together with a tight, shallow thermocline, overlying a thick, bottom boundary with weak stratification (Fig. 4a). There are cooler waters in the well-mixed region, which then result in a surface heat input of more than 100 W m^{-2} , greater than over the warmer, stratified waters offshore (Fig. 4b). This contrast between the well mixed and stratified waters, marked by the tidal-mixing front, changes location over the year, moving from more than 40 km offshore in winter to 20 km in summer (Fig. 4c). This boundary also migrates with the spring-neap cycle in tidal forcing, moving offshore when the mechanical forcing is stronger.

c. Transformation and formation rates in density space

First, consider a rough scaling for the transformation fluxes and, second, diagnostics from the suite of mixed-layer models; for numerical details, see the Appendix.

i. *Scaling for transformation rates for a tidal-mixing front.* The presence of a tidal-mixing front is associated with changes in air-sea fluxes and mixing across the front. Here, the cross-front and along-front scales are assumed to be typically 10 km and 100 km, respectively. The temperature contrast across a front leads to a change in the air-sea heat flux of 100 W m^{-2} , corresponding to a density flux of $D_{in} = -\frac{\alpha}{C_p} \mathcal{H}_{in} \sim 10^{-4} \text{ kg m}^{-2} \text{ s}^{-1}$, which implies a transformation rate of $G_{in} \sim 10^{-2} \text{ Sv}$.

For the diffusive flux of density from mixing, $D_{diff} = K_z \frac{\partial \sigma}{\partial z}$, there is a comparable contribution to that provided from air-sea fluxes, if the vertical diffusivity reaches $K_z \sim 10^{-3} \text{ m}^2 \text{ s}^{-1}$ and vertical density gradient, $\partial \sigma / \partial z \sim 0.1 \text{ kg m}^{-4}$. These values turn out to be plausible for the shallow shelf seas with strong tides.

Now consider the water-mass transformation associated with the migration of the tidal-mixing front, focussing on two periods, the warming and strengthening of stratification, as well as the cooling and weakening of stratification (Fig. 5a,c).

ii. *Transformation rates from the one-dimensional model.* In the warming phase, there is an overall transformation of $-30 \times 10^{-3} \text{ Sv}$ at $\sigma = 26.1$, directed from dense to light water (Fig. 5b). This transformation is primarily driven by the air-sea density fluxes, but is augmented by a diffusive transfer at $\sigma = 26.1$, associated with the strong diffusive density fluxes between the well mixed and stratified waters (Fig. 5a, shading).

In the cooling phase, there is an overall transformation of $18 \times 10^{-3} \text{ Sv}$ at $\sigma = 25.3$, directed from light to dense waters (Fig. 5d). At this time, there are comparable contributions

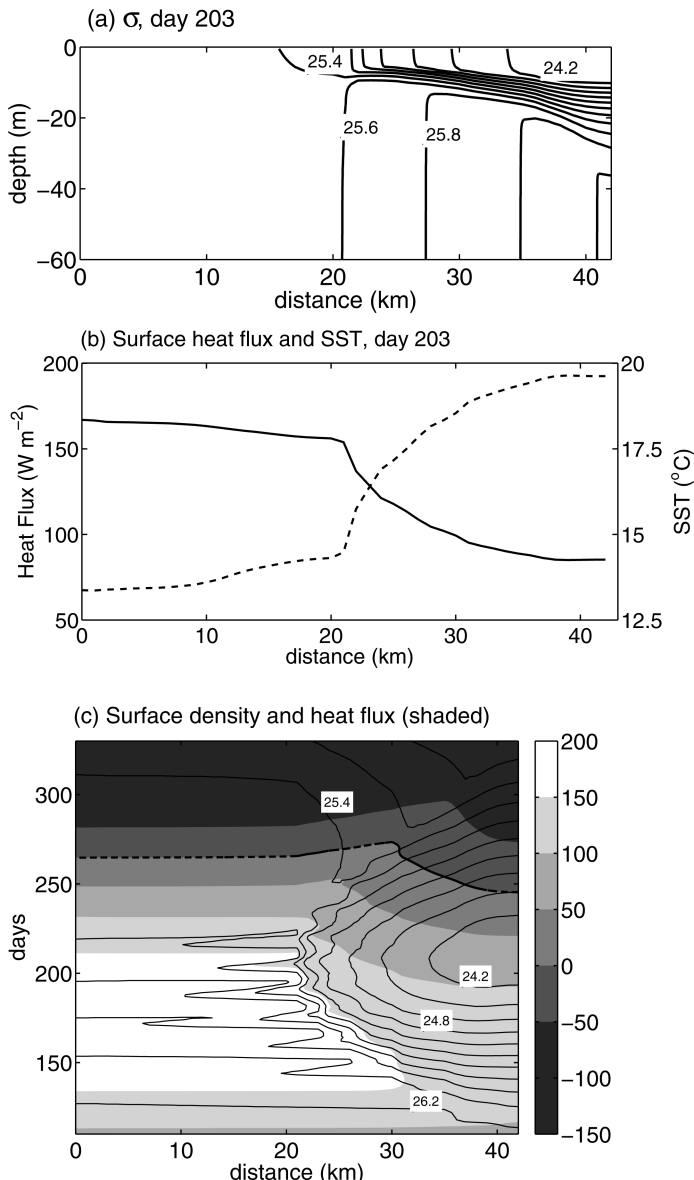


Figure 4. (a) Vertical section of σ versus distance from the coast during maximum stratification for day 203, diagnosed from the series of one-dimensional models. There are surface and bottom fronts separating the well mixed and stratified waters. (b) Surface heat flux into the ocean (W m^{-2} , full line) and surface temperature ($^{\circ}\text{C}$, dashed line) versus distance for day 203 revealing an increased heat input toward the coast due to the onshore decrease in surface temperature. (c) Surface σ (contours) and surface heat fluxes (W m^{-2} , shading) for time versus distance revealing the offshore emergence of stratification and the enhanced surface heat input in well-mixed waters; the dashed line represents the zero-line for the surface heat flux.

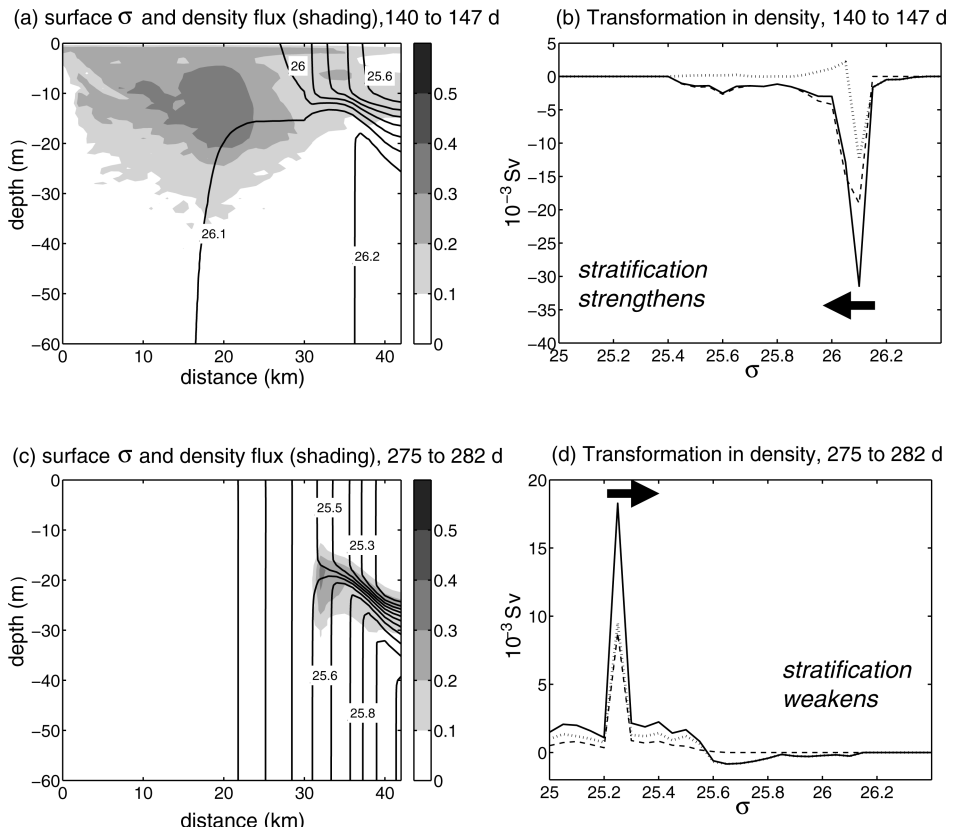


Figure 5. (a), (c), left panels: Sections of density (thick lines) and diffusive density fluxes ($10^{-5} \text{ kg m}^{-2} \text{ s}^{-1}$, shaded); (b), (d), right panels: Diapycnal volume flux or transformation rates (10^{-3} Sv) in density space (arrow indicates direction) when the stratification strengthens (days 140–147, top panels) and weakens (days 275–282, bottom panels). During the warming period, waters are transformed to lighter density classes (with a negative transformation, black arrow directed to the left) and the tidal-mixing front moving onshore. Conversely, in the cooling period, waters are transformed to denser classes (black arrow directed to the right) with the tidal-mixing front moving offshore. For the transformation rates, dashed lines represent the contributions from the air-sea fluxes, dotted lines represent the contributions from the diffusive fluxes, continuous lines represent the contributions from the sum of the air-sea and diffusive fluxes; note a change of scale in the axes.

from the air-sea and diffusive density contributions, both acting to increase the volume of the intermediate density classes.

The convergence of the transformation in density space gives the formation rate (1). During the warming phase, the negative transformation is expressed in terms of water-mass formation with an increase in the volume of lighter waters and a compensating decrease in the volume of denser waters (Fig. 6a). This pattern in formation rates reverse in the

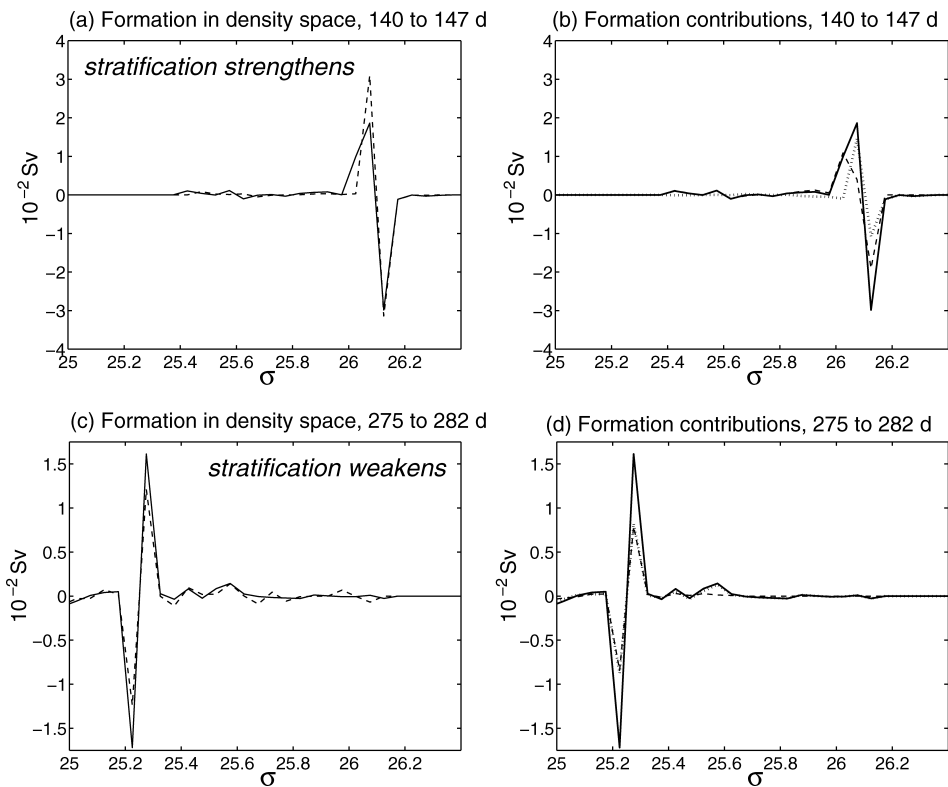


Figure 6. (a), (c), left panels: Formation rates (10^{-2} Sv) diagnosed using the Walin framework (full lines) and diagnosed directly from the changes in volume in the model (dashed lines) for the two periods when stratification strengthens or weakens; (b), (d), right panels: contributions to the formation rates (10^{-2} Sv) in the Walin framework from the air-sea fluxes (dashed lines), diffusive fluxes (dotted lines) and their sum (full lines); note the change of scale in the axes.

cooling phase (Fig. 6c). These estimates of formation from the sum of the contributions of air-sea fluxes and diapycnal mixing compare favorably with estimates made directly from the actual volumetric changes in the model (Fig. 6a,c); although the actual formation occurs in a slightly narrower density interval, than that diagnosed using the Walin framework.

For the formation rates, the effect of the air-sea fluxes and diffusive mixing become comparable in magnitude to each other (Fig. 6b,d). While for these two particular periods, both the air-sea and diffusive contributions tend to reinforce each other, this reinforcement does not generally hold in the same density class.

The diffusive contribution to the transformation generally reaches half the maximum amplitude of the air-sea contribution (Fig. 7a). The ratio of these contributions varies seasonally (Fig. 7b), but is not affected by the spring-neap cycle, as found by repeating the model integrations with only the M2 tidal cycle.

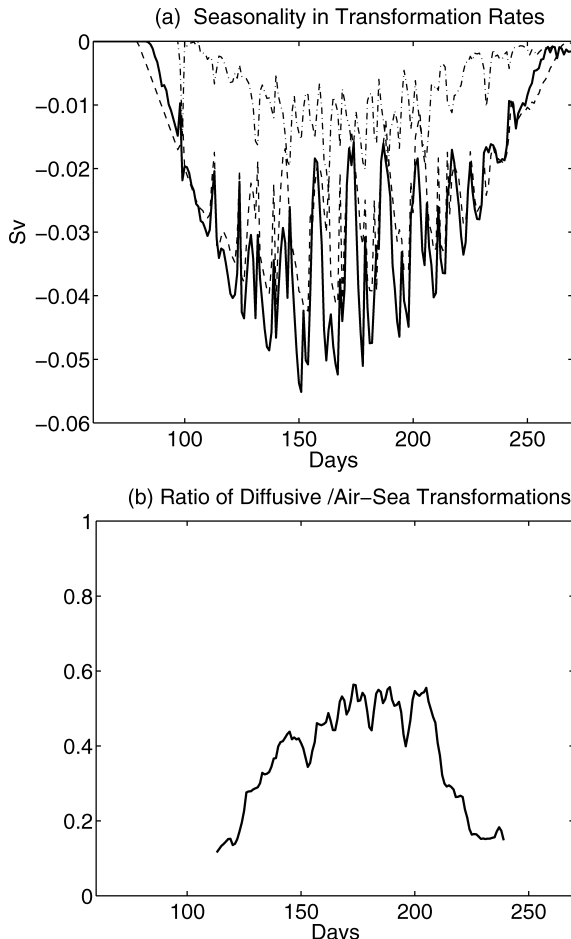


Figure 7. (a) Seasonal evolution of the maximum amplitude of the transformation rates (Sv). Contributions are from the air-sea fluxes (dashed lines) and diffusive fluxes (dot-dashed lines) together with their sum (full lines). (b) Seasonal evolution in the ratio between the maximum amplitude of the diffusive and air-sea fluxes components of the transformation rates. The ratio has been averaged over a 14-day period, corresponding to a spring-to-spring tidal period.

4. Implications for the transfer of nutrients across the tidal-mixing front

Walsh (1982) originally set out this diagnostic framework in temperature space, combining volume and heat budgets for an isothermal layer. This framework can equivalently be applied to any tracer, as long as any additional tracer sources and sinks are included. In this section, the framework is applied in nutrient space, where a volume and nutrient budget are applied for a layer between two nutrient surfaces, rather than between two density surfaces (Fig. 2). The rate of formation of water mass, $M(N)$, between the nutrient surfaces, N and

$N + \Delta N$, is defined as the convergence of the diapycnal volume fluxes directed across these nutrient surfaces, $G(N)$, given by

$$M(N)\Delta N = -\Delta N \frac{\partial G}{\partial N}. \quad (4)$$

By applying a nutrient budget similar to (2), the diapycnal volume flux or transformation, $G(N)$, in nutrient space is defined as

$$G(N) = -\frac{\partial D_{diff}(N)}{\partial N} - \frac{1}{\Delta N} \int \mathcal{U}_{net} dV + \frac{1}{\Delta N} \int_{outcrop} \mathcal{D}_N dA + \frac{1}{\Delta N} \int_{grounding} \mathcal{B}_N dA, \quad (5)$$

where $D_{diff}(N)$ is the diffusive flux of nutrients, $\mathcal{U}_{net} = \mathcal{U} + \mathcal{R}$ is the net nutrient uptake rate, where \mathcal{U} and \mathcal{R} are the rates of biological uptake and remineralization respectively, \mathcal{D}_N is the flux of nutrients at the outcrop of the nutrient layer, representing the air-sea flux and \mathcal{B}_N is the flux of nutrients at the grounding of the nutrient layer, representing the benthic flux. Due to its small contribution, air-sea fluxes of nutrients at the sea surface are subsequently neglected.

a. Nutrient and chlorophyll distributions

The seasonality in the physics leads to characteristic cycles in the nutrients and chlorophyll. There is a strong spring bloom in the shelf seas leading to a rapid consumption of nutrients in the surface waters in the stratified part of the shelf. Nutrients persist in having high concentrations below the thermocline in the stratified waters, as well as over the well-mixed waters due to the resupply of nutrients from the benthic boundary (Fig. 8a,b). This nutrient distribution then sustains a subsurface chlorophyll maximum during summer (Fig. 1). The migration of the tidal-mixing front is associated with a migration in the associated gradient in surface nutrient and depth-integrated chlorophyll concentrations (Fig. 8c,d).

b. Transformation and formation rates in nutrient space

Now again consider the water-mass transformation for the tidal-mixing front, but now evaluated in nutrient space, for the two periods of strengthening and weakening in stratification.

i. Transformation and formation rates in nutrient space in the one-dimensional numerical model. In the warming phase, the suite of mixed-layer models reveals a transformation of -8×10^{-3} Sv at $N = 6.9 \text{ mmol m}^{-3}$, directed from nutrient-rich to nutrient-depleted waters (Fig. 9a). This transformation is driven by the biological consumption associated with the spring bloom. In the cooling phase, there is the reverse transformation, 3.2×10^{-2} Sv at $N = 4 \text{ mmol m}^{-3}$, directed from nutrient-depleted to nutrient-rich waters (Fig. 9b). This transformation is controlled primarily by the diffusive contribution, rather than by the biological recycling.

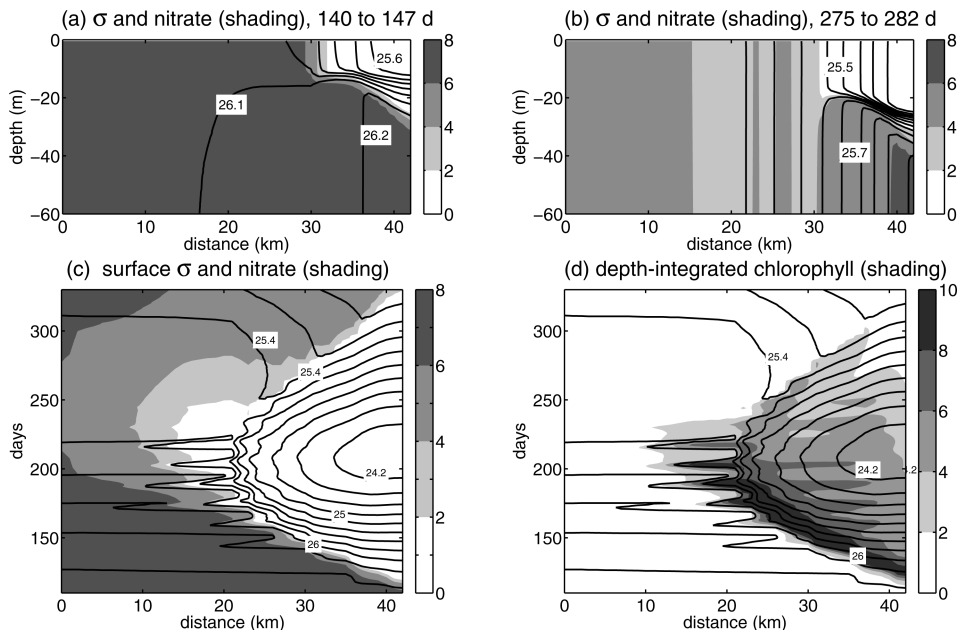


Figure 8. Top panels, (a) and (b): vertical sections of σ (contours) and nitrate concentration (mmol m^{-3} , shaded) when stratification strengthens or weakens. Bottom panels, (c) and (d): density (contours) with surface nitrate concentration (mmol m^{-3} , shaded) or depth-integrated chlorophyll concentration (mg Chl m^{-3} , shaded) for time versus distance revealing nitrate-rich well mixed waters, but greater depth-integrated chlorophyll concentrations along the tidal-mixing front and thermocline.

The convergence of the transformation in nutrient space leads to the formation rate in nutrient space (4). During the warming phase, biological consumption drives the increase in the volume of nutrient-depleted waters (Fig. 10a,b). During the cooling phase, the reverse occurs where mixing drives the formation of nutrient-rich waters (Fig. 10c,d).

Our estimates of water-mass formation in nutrient space within this model environment again compare favorably with direct diagnostics of the volume changes (Fig. 10a,c).

ii. Relationship between transformation and formation rates in density and nutrient spaces. The transformation rates in density and nutrient space differ according to the different processes affecting transformation in each co-ordinate system, as well as depending on the relative size of the temperature and density bins. For the period where stratification is increasing, the ratio of the maximum transformations in density and nutrient space, $\Delta G_\sigma / \Delta G_N$, reaches ~ 4 , while in the period when stratification weakens, $\Delta G_\sigma / \Delta G_N$, instead reaches 0.5 (Figs. 5 and 9).

In principle, a simple relationship between the density and nutrient concentration allows one to convert the transformation rates in density to that in nutrient. However, the

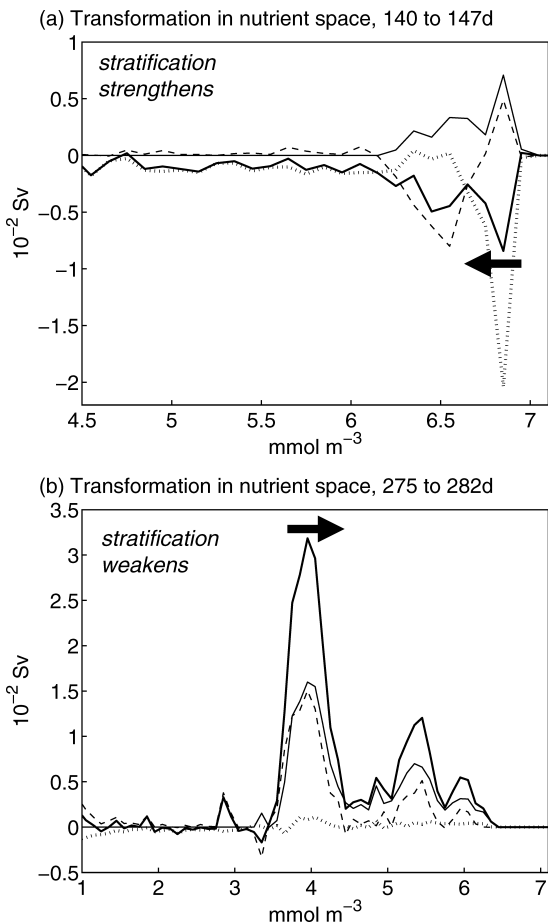


Figure 9. Transformation rates (10^{-2} Sv) in nutrient space (arrow indicates direction) when stratification either (a) strengthens or (b) weakens. During the warming period, there is a transformation of nutrient-rich to nutrient-poor waters (black arrow directed to the left), sustaining subsequent biological consumption. During the cooling period, there is an opposing conversion of waters with intermediate nutrient concentrations to more nutrient-rich waters (black arrow directed to the right). Contributions are from the diffusive fluxes (thick dashed lines), the biological consumption and remineralisation (thin dotted lines), benthic fluxes (thin full line) and their sum (thick full line); note the change of scale of the axes.

transformation in density and nutrient space are most closely related in the spring, when there is a relatively tight relationship between density and nutrient concentration (Fig. 8a). During the summer and autumn, the relationship between the distributions of density and nutrient concentration alter through nutrient concentrations being increased in light waters by physical transformation, as well as reduced in surface waters by biological consumption (Fig. 8b,c).

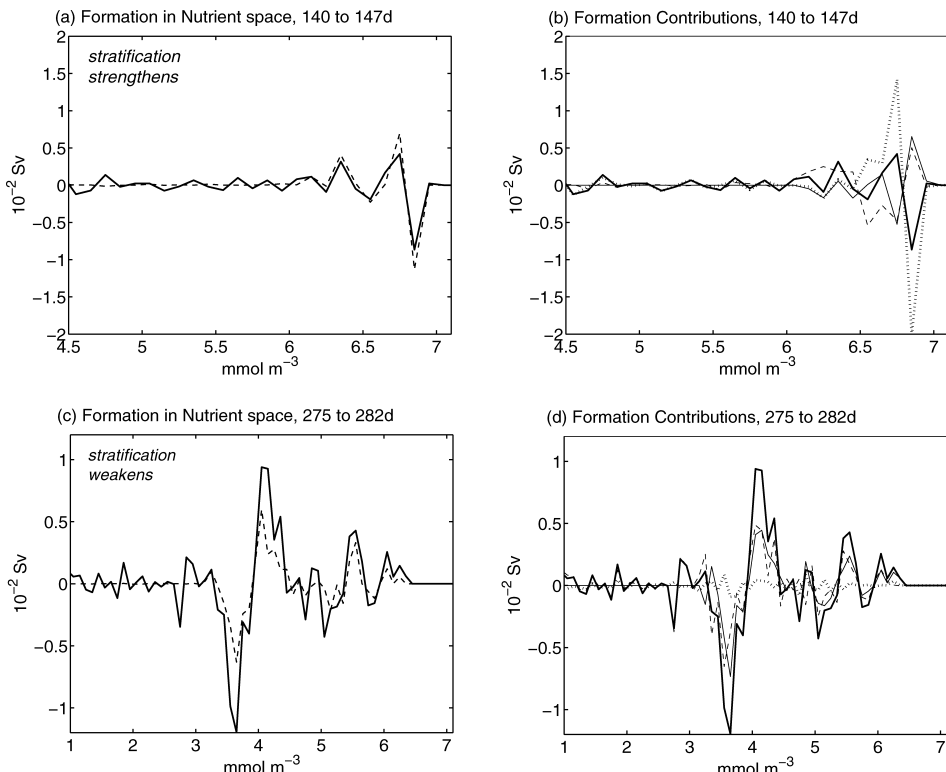


Figure 10. (a), (c), left panels: Formation rates in nutrient space (10^{-2} Sv) diagnosed from the Walin framework (full lines) and directly from the change in volume between these nutrient surfaces (dashed lines). During the warming phase, there is a loss of nutrient-rich waters, linked to the transformation to nutrient-poor waters. Conversely, during the cooling phase, there is a loss of waters with intermediate nutrient concentrations and a gain in volume of more nutrient-rich waters; (b), (d), right panels: Contributions to the formation rates (10^{-2} Sv) for both periods from the diffusive fluxes (dashed lines), the biological consumption and remineralization (dotted lines) and the benthic fluxes (thin continuous lines); note the change of scale of the axes.

5. Data estimates of the water-mass transformation at the shelf break front

Given that the transformation across a modeled tidal-mixing front can be estimated through knowledge of the air-sea fluxes and tidal mixing, now consider the more challenging problem of the transformation across the shelf-break front using available air-sea flux data, surface density data and estimates of *in situ* mixing.

a. Temperature and salinity fields

Sea surface temperature (SST) are obtained from 15 days satellite (AVHRR) composites, covering the period 15 December 2002 to 31 December 2003, over the Celtic Seas at

approximately 1.1 km resolution, covering the meridional section in Figure 1. Composites for SST reveal coldest waters at the end of winter, from 13 to 26 March 2003 (Fig. 11a) and warmest waters at the end of summer, 11 to 24 September 2003 (Fig. 11b). The shelf-break front is revealed by the band of cold waters aligned with isobaths (Fig. 11b, white lines) associated with the mixing from the baroclinic tide breaking at the shelf edge (Pingree and Mardell, 1981; Sharples *et al.*, 2007).

Salinity and the interior temperature distributions across the shelf break are taken from 9 CTD casts on 21 July 2005 (Fig. 11a,b, asterisks). The remotely-sensed SST were averaged over the center of the CTD casts using bins of the size of $1^\circ \times 1^\circ$. Surface density is then diagnosed from the remotely-sensed SST combined with salinity from the CTD casts for July; the density is interpolated to daily values, relying upon salinity not varying significantly seasonally and inter-annually.

The seasonality in surface temperature leads to a pronounced seasonal migration in surface density, ranging from $\sigma = 27.2$ in the region of the shelf break in March and lightening to $\sigma = 25.5$ by September (Fig. 11c). Over the center of the shelf break, there are slightly denser waters associated with the enhanced mixing at 48.25°N in Figure 11c.

b. Air-sea fluxes

The meteorological data are obtained from ECMWF re-analysis consisting of 6 hourly data centered at 50°N , 7°W . The air-sea fluxes are then calculated using bulk formulae (Gill, 1982) over the entire domain, including spatial variations in SST, but otherwise the atmospheric properties are assumed spatially uniform. The re-analysis meteorological forcing data are interpolated daily in order to combine with the daily SST fields.

c. Mixing regimes

To estimate the mixing contribution to the transformation rates, three different regimes are assumed:

- 1) an open ocean regime, in which $K_z \sim 10^{-5} \text{ m}^2 \text{ s}^{-1}$ is assumed over the vertical profile (Lewis *et al.*, 1986; Planas *et al.*, 1999), which is combined with a vertical density profile from a CTD cast on the open ocean side of the shelf break (Fig. 11a,b, lower-left asterisk);
- 2) a shelf break frontal regime, in which K_z is measured at the shelf edge ($48^\circ 34.3^\circ\text{N}$, $9^\circ 30.6^\circ\text{W}$, Fig. 11a,b, left panels, cross) in July 2005, which is combined with the coincident vertical density profile from the CTD cast;
- 3) a shelf sea regime, in which K_z and the vertical density profile are taken from the stratified shelf region of the numerical model considered in Section 3.

In each case, the K_z and density profiles from the observations and the numerical model were averaged for a spring-neap period. The profiles of K_z were finally mapped in density space after a vertical interpolation every 10 m.

While the SST analysis and mixing profiles are for different years, turbulence measurements were made in 2003 for a neap tide, but these measurements are then an underestimate

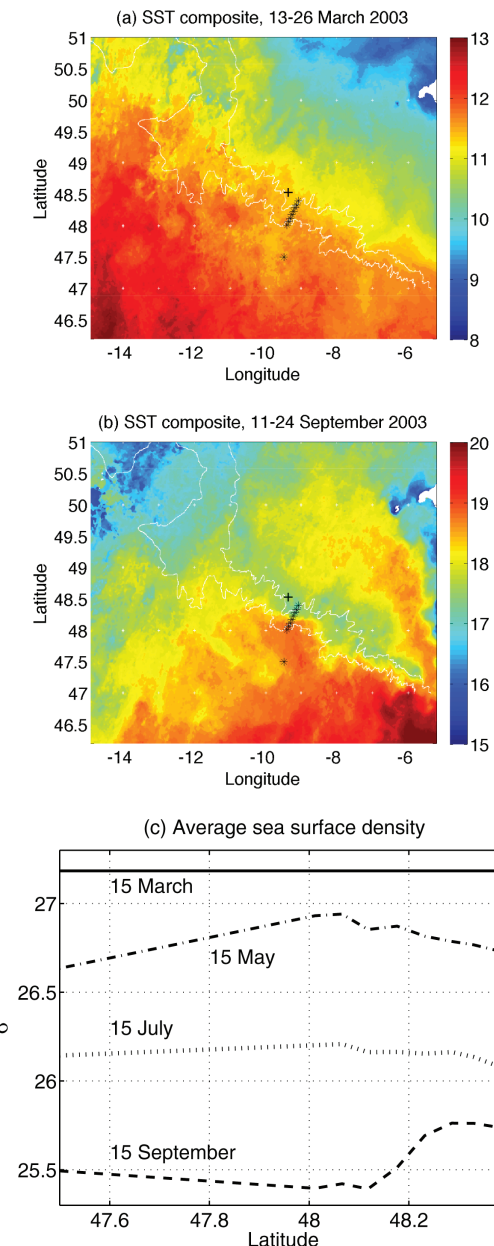


Figure 11. Satellite (AVHRR) composite of SST for the periods (a) from 13 to 26 March 2003, (b) from 11 to 24 September 2003. The shelf break is marked by thin white lines, CTD casts by black asterisks and where the vertical diffusivity was measured by black crosses. (c) Density along the cross-front section for 15 March 2003 (full line) and 15 September 2003 (dashed line).

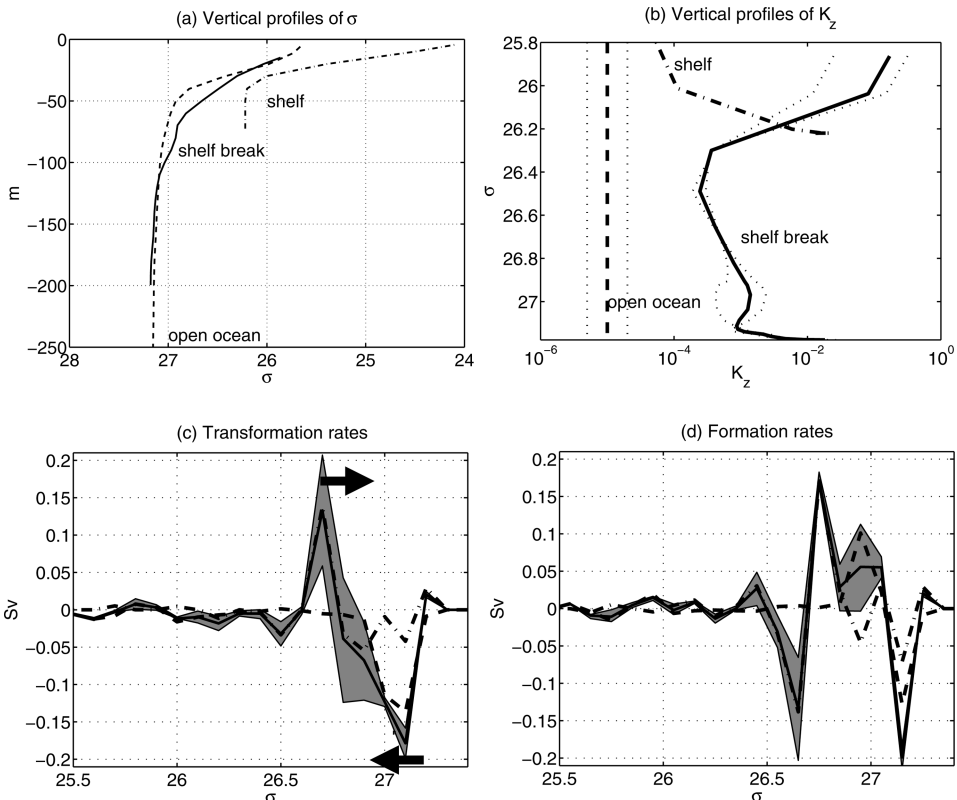


Figure 12. (a) Vertical profile of density at the shelf break front; (b) Profile of K_z ($\text{m}^2 \text{s}^{-1}$) as a function of density at the shelf break front; (c) Transformation rates (arrow indicates direction) and (d) formation rates (S_V) for the shelf-break region evaluated from 15 March to 15 September. Dashed lines indicate the air-sea component, dot-dashed lines indicate the mixing component and full lines indicate their sum. Shading represents uncertainties in the diagnostics, see main text for choices made.

for the mixing at the shelf edge. Instead, a cross-shelf edge transect in 2005 is used, based upon 90 profiles of turbulent diffusivity: 40 profiles over a 25-hour period for a neap tide and 50 profiles over a 25-hour period for a spring tide (Sharples *et al.*, 2007). At the same time, the 2005 transect revealed the same frontal structure across the shelf edge as in 2003, and the cool band of water in summer SST images is consistent between all years.

At the shelf break, there are very high values of diffusivity, with the mean profile representing an average based on dissipation rate measurements over spring and neap tidal cycles (Sharples *et al.*, 2007). Diffusivities reach $5 \times 10^{-2} \text{ m}^2 \text{s}^{-1}$ in the bottom water, and greater than $10^{-1} \text{ m}^2 \text{s}^{-1}$ toward the surface. Diffusivities are a minimum in the thermocline, at about $7 \times 10^{-3} \text{ m}^2 \text{s}^{-1}$ (Fig. 12a,b).

d. Estimates of transformation and formation rates

In order to estimate the transformation rates, the section across the shelf break is taken to be representative of the front with an along-front length of 100 km. These estimates can be scaled by a factor of 5 for the Celtic Sea, as the shelf break front extends for at least 500 km in Figure 11b; however, a smaller scale is taken for convenience and is consistent with the density distribution being assumed coherent along the front.

Uncertainties have been calculated for the transformation and formation rates adding a $\pm 5 \text{ W m}^{-2}$ uncertainty to the surface fluxes; making K_z vary for the open ocean transect between $0.5 \times 10^{-5} \text{ m}^2 \text{ s}^{-1}$ and $2 \times 10^{-5} \text{ m}^2 \text{ s}^{-1}$ (Lewis *et al.*, 1986; Planas *et al.*, 1999); and making K_z vary at the shelf break between the values measured for the separate neap and spring tides (Sharples *et al.*, 2007).

By combining the air-sea and mixing contributions, the transformation reaches -0.18 Sv at $\sigma = 27.1$, directed toward lighter waters, and 0.14 Sv at $\sigma = 26.7$, directed to denser waters (Fig. 12c, full line). This transformation reaching a magnitude of 0.2 Sv is equivalent to a cross-front velocity of 1 cm s^{-1} assuming a transformation across a front extending over 100 km and a vertical scale of 200 m.

These transformation rates then correspond to a formation rate of 0.16 Sv at $\sigma = 26.75$, representing more water formed in this density class, as well as -0.14 Sv at $\sigma = 26.55$ and of -0.2 Sv at $\sigma = 27.15$, representing a loss of water (Fig. 12d, full line).

Seasonal heating leads to the transformation of dense water to light water at $\sigma = 27.1$ (Fig. 12c, dashed line). Conversely, mixing leads to the transformation of lighter to denser waters at $\sigma = 26.7$, which then leads to the water-mass formation at $\sigma = 26.75$ and consumption at $\sigma = 26.55$ (Fig. 12c,d, dot-dashed line). At $\sigma = 27.15$, water masses are eroded due to both the surface fluxes and mixing.

e. Implications of the transformation for the nutrient budget

During the summer, nutrients are generally depleted over the light, surface waters, but increase in concentration over the denser waters, as revealed in the section taken across the shelf break in July 2005 (Fig. 13a) (Sharples *et al.*, 2007). In the same manner as the previous calculations, the transformation rates driven by the air-sea forcing and mixing are again evaluated, but now just for the period 1 to 18 July: air-sea fluxes drive a transformation reaching -0.05 Sv at $\sigma = 26.1$ directed to lighter σ , while diapycnal mixing drives a transformation reaching 0.14 Sv at $\sigma = 26.7$ and -0.04 Sv at $\sigma = 27.1$, directed to denser and lighter surfaces respectively (Fig. 13b). Accordingly, there is the peak in formation rate of 0.16 Sv at $\sigma = 26.75$ (Fig. 13c).

Given this transformation in density space, what then are the implications for the nutrient transfer? Applying a nutrient budget like (2) within two density surface (Fig. 2b), assuming the N surfaces are aligned with ρ (as in Fig. 13a), gives

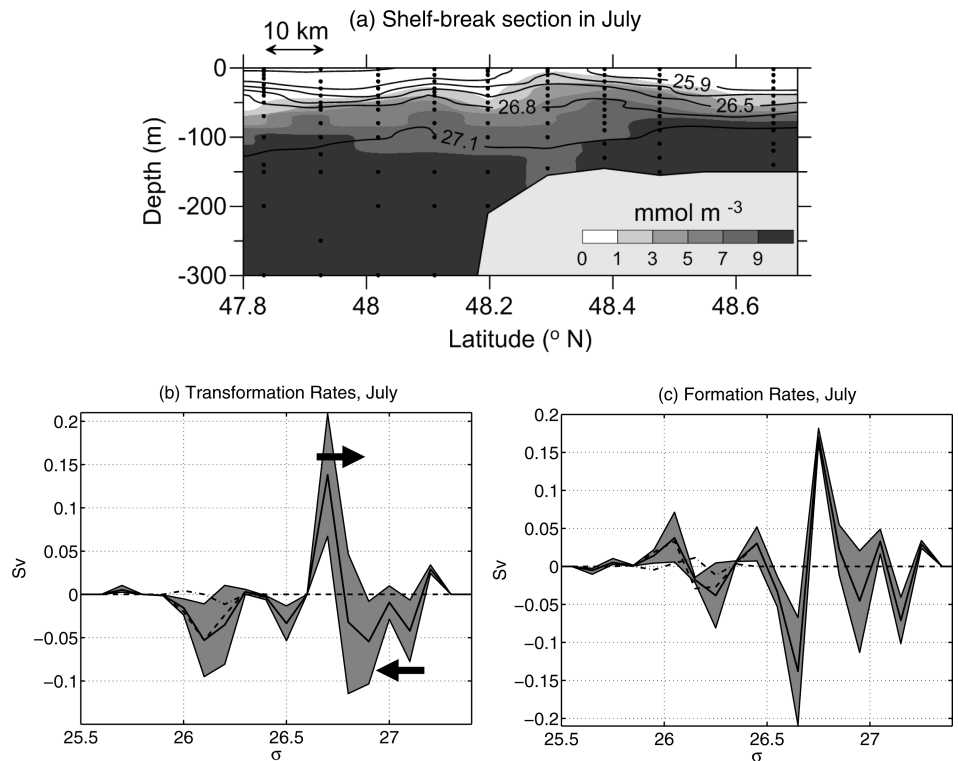


Figure 13. (a) Section of density at the shelf break front and nitrate concentration (shaded, mmol m^{-3}) for July 2005; (b) Transformation rates (arrow indicates direction) and (c) formation rates (Sv) for the shelf-break region evaluated from 1 to 18 July. Dashed lines indicate the air-sea component, dot-dashed lines indicate the mixing component and full lines indicate their sum. Shading represents uncertainties in the diagnostics, see main text for choices made.

$$\left(\frac{\partial \Delta V}{\partial t} + \Delta \Psi - \Delta \Psi_{P-E} \right) N = -\Delta \rho \frac{\partial}{\partial \rho} (GN) - \Delta \rho \frac{\partial D_{diff}^N}{\partial \rho} - \int_{V(\rho)} \mathcal{U}_{net} dV + \int_{A(\rho)} (\mathcal{D}_N + \mathcal{B}_N) dA, \quad (6)$$

where the nutrient terms are as in (5), but now defined within density surfaces and $V(\rho)$ and $A(\rho)$ represents the volume and bounding area of the density layer. Then for a steady state and no outflux of nutrients from the domain or exchange through the surface and bottom boundaries, the convergence of this diapycnal nutrient flux, GN , from the product of the transformation in density space and nutrient concentration, together with the diffusion of nutrient, D_{diff}^N , can support net biological uptake of nutrients,

$$-\Delta\rho \frac{\partial}{\partial\rho}(GN) \simeq \Delta\rho \frac{\partial D_{diff}^N}{\partial\rho} + \int_{V(\rho)} \mathcal{U}_{net} dV. \quad (7)$$

The first term on the left-hand side represents the convergence of the product of the transformation and nutrient concentration, which is partly driven by the diffusive flux of density from the mixing at the shelf (Fig. 13b, dot-dashed line). The first term on the right-hand side represents the change in the diffusive flux of nutrients across density surfaces, while the second term on the right-hand side represents the net biological uptake, \mathcal{U}_{net} , positive for a loss of nutrients, over the volume V enclosed between the bounding density surfaces, ρ to $\rho + \Delta\rho$.

This diapycnal nutrient flux, GN , at $\sigma = 26.7$ is $0.14 \text{ Sv} \times 4.6 \text{ mmol N m}^{-3}$ and at $\sigma = 27.1$ is $-0.04 \text{ Sv} \times 10.1 \text{ mmol N m}^{-3}$, which implies a nitrate supply of $1.05 \times 10^3 \text{ mol N s}^{-1}$ over the σ range 26.7 to 27.1 from mixing generated by the internal tide using (6). Assuming a horizontal area of 150 km by 100 km for the shelf break, then allows this nutrient supply over the entire shelf break to be converted into a nutrient supply per unit horizontal area of $6 \text{ mmol N m}^{-2} \text{ d}^{-1}$; this estimate is consistent with direct estimate from the mixing, which peaks at a spring tide of $9 \text{ mmol N m}^{-2} \text{ d}^{-1}$ and reduces at a neap tide to $1 \text{ mmol N m}^{-2} \text{ d}^{-1}$ (Sharples *et al.*, 2007).

In principle, this approach can then be extended for different periods of the year, combining with the transformation contributions from the air-sea forcing, in order to estimate the nutrient supply made available to different density classes, which then sustains subsequent biological consumption.

6. Conclusions

The Walin (1982) formulation provides an integrated framework to understand how water masses are converted from one density class to another in the shelf seas through a combination of surface density fluxes and mechanical mixing. Unlike the open ocean, the water-mass formation regions in the shelf seas experience both strong air-sea forcing and mixing from the mechanical forcing of tidal flows interacting with the sea floor.

The shelf seas are separated into different regions by fronts, the tidally-mixed front separating well-mixed waters and stratified waters over the shelf in summer, and the shelf-break front separating the shelf and the open ocean. In our model assessments, the Walin framework can be utilized to estimate the water-mass transformation and formations rates for the tidally-mixed front subject to knowledge of the air-sea fluxes and mixing. This framework can be further generalized to evaluate the biological consumption subject to knowledge of the nutrient transformation and diffusive flux of nutrients. For the shelf-break front, the data analyses provide plausible estimates for the water-mass conversion and nutrient supply for biological consumption subject to knowledge of the air-sea fluxes, diapycnal mixing and nutrient concentrations within density layers.

This water-mass conversion in the shelf seas is important for several reasons: in high latitudes, the formation of cold, dense waters leads to cascading, forming dense overflow

waters spreading into the open ocean (Ivanov *et al.*, 2004); the influx of open ocean waters provides an influx of nutrients into the shelf seas, which helps sustain the enhanced productivity in coastal waters; and, in turn, the productivity of the shelf seas provides a potentially important drawdown of atmospheric carbon dioxide (Thomas *et al.*, 2004; Baschek *et al.*, 2006).

Many of the controlling processes in the shelf seas occur on fine horizontal scales, involving frontal contrasts in mixing and time-dependent circulations. While these detailed processes are difficult to monitor in a systematic way, this Walin framework provides a potentially attractive way to provide an integrated view of how the water masses are transformed, as well as their possible influence on the cycling of nutrients and carbon.

APPENDIX

Numerical Evaluation of Transformation and Formation Rates

a. Transformation and formation rates in density space

The transformation and formation rates in density space is evaluated following Marshall *et al.* (1999). The results for the transformation and formation rates depend on the choice of the density bin. In this study a density bin of $\Delta\rho = 0.05 \text{ kg m}^{-3}$ has been used; this choice led to the optimal agreement between the volume rates and the formation rates diagnosed from the Walin (1982) framework and directly from the model.

i. *Volume balance.* For a certain potential density class ρ_0 and for a certain time t , the volume of fluid $\Delta V(\rho_0; t)$, bound by the ρ_0 and $\rho_0 + \Delta\rho$ isopycnals, is calculated as the sum of the infinitesimal volumes included between ρ_0 and $\rho_0 + \Delta\rho$:

$$\Delta V(\rho_0; t) = \left(\sum_{i,k} dx dz \times \Pi_V[\rho_0; \rho(i, k; t)] \right) L_y, \quad (8)$$

where i and k represent the horizontal and vertical co-ordinate indexes respectively and the boxcar function $\Pi_V[\rho_0; \rho(i, k; t)]$ is defined as

$$\Pi_V[\rho_0; \rho(i, k; t)] = \begin{cases} 1 & \text{if } \rho_0 \leq \rho < \rho_0 + \Delta\rho \\ 0 & \text{otherwise,} \end{cases} \quad (9)$$

so that $\Delta V(\rho_0; t)$ is defined at $\rho_0 + \frac{\Delta\rho}{2}$. The volume rate for a time interval $\tau = t_1 - t_0$, which appears on the l.h.s. of (1), can be thus calculated setting $\Delta\Psi = 0$ and $\Delta\Psi_{P-E} = 0$, due to the closed domain and to the lack of volume input and output due to freshwater fluxes, and $(\Delta V(\rho_0; t_1) - \Delta V(\rho_0; t_0))/\tau$.

ii. *Air-sea component.* The air-sea density flux, $\mathcal{D}_{in} = -\frac{\alpha_T}{C_p} \mathcal{H} + \rho\beta_S S(\mathcal{E} - \mathcal{P})$ in units of $\text{kg m}^{-2} \text{ s}^{-1}$, drives a water-mass transformation, $G_{air-sea}(\rho_0; t) = \frac{1}{\Delta\rho} \int_{outcrop} \mathcal{D}_{in} dA$, given by the second term at the r.h.s. of (3),

$$G_{air-sea}(\rho_0; \tau) = \frac{1}{\tau} \sum_t \left[\frac{1}{\Delta\rho} \left(\sum_i \mathcal{D}_{in}(i; t) dx \times \Pi_{air-sea}[\rho_0; \rho(i; t)] \right) L_y \right] \Delta t, \quad (10)$$

which is evaluated for a particular potential density class ρ_0 and time interval $\tau = t_1 - t_0$, as represented by a boxcar function $\Pi_{air-sea}[\rho_0; \rho(i; t)]$ defined as

$$\Pi_{air-sea}[\rho_0; \rho(i; t)] = \begin{cases} 1 & \text{if } \rho_0 - \Delta\rho/2 < \rho < \rho_0 + \Delta\rho/2 \\ 0 & \text{otherwise.} \end{cases} \quad (11)$$

Given the air-sea component of the transformation rate for two different outcropping isopycnals, ρ_0 and $\rho_0 + \Delta\rho$, the air-sea component of the formation rate $M_{air-sea}\Delta\rho$, given by the r.h.s. of (1), is calculated as

$$M_{air-sea}(\rho_0 + \Delta\rho/2; \tau) = \frac{1}{\tau} \sum_t [G_{air-sea}(\rho_0 + \Delta\rho; \tau) - G_{air-sea}(\rho_0; \tau)] \Delta t, \quad (12)$$

so that $M_{air-sea}(\rho_0 + \Delta\rho/2; \tau)$ is defined at $\rho_0 + \frac{\Delta\rho}{2}$, in agreement with the calculations for the volume rate.

iii. Diffusive component. The diffusive flux from mixing, $D_{diff} = K_z \frac{\partial \rho}{\partial z}$ in units of $\text{kg m}^{-2} \text{s}^{-1}$, leads to a transformation, $G_{diff}(\rho_0; t)$, given by the first term at the r.h.s. of (3),

$$G_{diff}(\rho_0; \tau) = \frac{1}{\tau} \sum_t \left[\frac{1}{\Delta\rho} \left(\sum_{i,k} \mathcal{D}_{diff} \left(i, k + \frac{1}{2}; t \right) dx dz \right. \right. \\ \left. \left. \times \Pi_{diff} \left[\rho_0; \rho \left(i, k + \frac{1}{2}; t \right) \right] \right) L_y \right] \Delta t, \quad (13)$$

which applies for a particular potential density class ρ_0 and time interval $\tau = t_1 - t_0$, with the boxcar function $\Pi_{diff}[\rho_0; \rho(i, k + \frac{1}{2}; t)]$ defined in the same way as in (11).

In analogy with the air-sea component, the diffusive component of the formation rate $M_{diff}\Delta\rho$ is calculated as

$$M_{diff}(\rho_0 + \Delta\rho/2; \tau) = \frac{1}{\tau} \sum_t [G_{diff}(\rho_0 + \Delta\rho; \tau) - G_{diff}(\rho_0; \tau)] \Delta t, \quad (14)$$

so that $M_{diff}(\rho_0 + \Delta\rho/2; \tau)$ is defined at $\rho_0 + \frac{\Delta\rho}{2}$, in agreement with the calculations for the volume rate.

b. Transformation and formation rates in nutrient space

The calculation of the volume rate and of the diffusive components of the transformation and formation rates in nutrient space are calculated in an analogous way than in the density space, replacing the density class ρ_0 with a nutrient concentration class N_0 . In all the calculations, the value $\Delta N = 0.1 \text{ mmol m}^{-3}$ has been used.

i. *Biological uptake component.* The net biological uptake component of the water mass transformation, given by the second term at the r.h.s. of (5), is calculated as

$$G_{U_{net}}(N_0; \tau) = \frac{1}{\tau} \sum_t \left[\frac{1}{\Delta N} \left(\sum_{i,k} \mathcal{U}_{net}(i, k; t) dx dz \times \Pi_{U_{net}}[N_0; N(i, k; t)] \right) L_y \right] \Delta t, \quad (15)$$

which is for a particular nutrient concentration class N_0 and time interval $\tau = t_1 - t_0$, as represented by the boxcar function $\Pi_{U_{net}}[N_0; N(i, k; t)]$ as in (11).

The net uptake component of the formation rate $M_{U_{net}} \Delta N$, given by the r.h.s. of (4), is then calculated as

$$M_{U_{net}}(N_0 + \Delta N/2; \tau) = \frac{1}{\tau} \sum_t [G_{U_{net}}(N_0 + \Delta N; \tau) - G_{U_{net}}(N_0; \tau)] \Delta t, \quad (16)$$

so that $M_{U_{net}}(N_0 + \Delta N/2; \tau)$ is defined at $N_0 + \frac{\Delta N}{2}$.

ii. *Benthic component.* The benthic nutrient flux \mathcal{B}_N is calculated as a relaxation of the nutrient concentration at the bottom of the grid

$$\mathcal{B}_N = D \left(1 - \frac{N}{N_0} \right), \quad (17)$$

where D is the maximum possible flux of nutrients out of the sediments, set here as $10 \text{ mmol m}^{-2} \text{ days}^{-1}$ and N_0 is the constant value of DIN that the model relaxes to, here set as 7 mmol m^{-3} (Sharples, 2008).

The benthic component of the water mass transformation $G_{benthic}(N_0; t) = \frac{1}{\Delta N} \int_{grounding} \mathcal{B}_N dA$, given by the last term at the r.h.s. of (5), is calculated as

$$G_{benthic}(N_0; \tau) = \frac{1}{\tau} \sum_t \left[\frac{1}{\Delta N} \left(\sum_i \mathcal{B}_N(i; t) dx \times \Pi_{benthic}[N_0; N(i; t)] \right) L_y \right] \Delta t, \quad (18)$$

which is defined for a particular nutrient concentration class N_0 and time interval $\tau = t_1 - t_0$, as represented by the boxcar function $\Pi_{benthic}[N_0; N(i; t)]$ as in (11).

Given the benthic component of the transformation rate for two different grounding nutrient surfaces, N_0 and $N_0 + \Delta N$, the benthic component of the formation rate $M_{benthic} \Delta N$ is calculated as

$$M_{benthic}(N_0 + \Delta N/2; \tau) = \frac{1}{\tau} \sum_t [G_{benthic}(N_0 + \Delta N; \tau) - G_{benthic}(N_0; \tau)] \Delta t, \quad (19)$$

so that $M_{benthic}(N_0 + \Delta N/2; \tau)$ is defined at $N_0 + \frac{\Delta N}{2}$, in agreement with the calculations for the volume rate.

c. Model grid

The transformation and formation rates are evaluated for a tidally-mixed front with along front and depth scales of $L_y = 10^4$ m and $h = 80$ m, respectively using levels every 1 m in the vertical.

The one-dimensional numerical model does not use a cross-front co-ordinate in distance, but instead uses the parameter $\log_{10}(h/U^3)$, where h is depth and U is the speed of the tidal currents, which varies in the range $U = 0.1$ m s $^{-1}$ and $U = 1$ m s $^{-1}$, defining whether the water column is tidally mixed or stratified (Simpson and Hunter, 1974). The resolution of the one-dimensional numerical model across the front is typically 0.04 units of $\log_{10}(h/U^3)$, comparable with observed gradients from 0.02 and 0.06 in the same units in the shelf seas (Pingree and Griffiths, 1978), which is equivalent to a choice of $dx = 10^3$ m and 43 grid points in the horizontal.

Acknowledgments. This study was supported by the UK Natural Environment Research Council (Grant NE/D011108/1). Sea surface temperature data were obtained from the NERC Earth Observation Data Acquisition and Analysis Service (NEODAAS) of the Plymouth Marine Laboratory.

REFERENCES

- Badin, G. and R. G. Williams. 2010. On the buoyancy forcing and residual circulation in the Southern Ocean: the feedback from Ekman and eddy transfer. *J. Phys. Oceanogr.*, *40*, 295–310.
- Badin, G., R. G. Williams, J. T. Holt, and L. Fernand. 2009. Are mesoscale eddies in shelf seas formed by baroclinic instability of tidal fronts? *J. Geophys. Res.*, *114*, C10021, doi:10.1029/2009JC005340.
- Baschek, B., D. M. Farmer, and C. Garrett. 2006. Tidal fronts and their role in air-sea gas exchange. *J. Mar. Res.*, *64*, 483–515.
- Canuto, V. M., A. Howard, Y. Cheng, and M. S. Dubovikov. 2001. Ocean turbulence. Part I: One-point closure model - Momentum and heat vertical diffusivities. *J. Phys. Oceanogr.*, *31*, 1413–1426.
- Gill, A. E. 1982. *Atmosphere-Ocean Dynamics*, *30*, in International Geophysical Series, Academic Press, London, 662 pp.
- Ivanov, V. V., G. I. Shapiro, J. M. Huthnance, D. L. Aleynik, and P. N. Golovin. 2004. Cascades of dense water around the world ocean. *Prog. Oceanogr.*, *60*, 47–98.
- Lewis, M. R., W. G. Harrison, N. S. Oakey, D. Hebert, and T. Platt. 1986. Vertical nitrate fluxes in the oligotrophic ocean. *Science*, *234*, 870–873.

- Loder, J. W. and T. Platt. 1985. Physical controls on phytoplankton production at tidal fronts, in Proceedings of the 19th European Marine Biology Symposium, P. E. Gibbs, ed., Cambridge University Press, 3–21.
- MacCready, P. and W. R. Geyer. 2001. Estuarine salt flux through an isohaline surface. *J. Geophys. Res.*, *106*, 11629–11637.
- MacCready, P., R. D. Hetland, and W. R. Geyer. 2002. Long-term isohaline salt balance in an estuary. *Cont. Shelf Res.*, *22*, 1591–1601.
- Marshall, D. P. 1997. Subduction of water masses in an eddying ocean. *J. Mar. Res.*, *55*, 201–222.
- Marshall, J., D. Jamous, and J. Nilsson. 1999. Reconciling thermodynamic and dynamic methods of computation of water-mass transformation rates. *Deep-Sea Res. I*, *46*, 545–572.
- Nurser, A. J. G., R. Marsh, and R. G. Williams. 1999. Diagnosing water mass formation from air-sea fluxes and surface mixing. *J. Phys. Oceanogr.*, *29*, 1468–1487.
- Pingree, R. D. and D. K. Griffiths. 1978. Tidal fronts on shelf seas around British Isles. *J. Geophys. Res.*, *83*, 4615–4622.
- Pingree, R. D. and G. T. Mardell. 1981. Slope turbulence, internal waves and phytoplankton growth at the Celtic Sea shelfbreak. *Proc. R. Soc. Lond. A*, *A302*, 663–682.
- Planas, D., S. Agusti, C. M. Duarte, T. C. Granata, and M. Merino. 1999. Nitrate uptake and diffusive nitrate supply in the central Atlantic. *Limnol. Oceanogr.*, *44*, 116–126.
- Sharples, J. 2008. Potential impacts of the spring-neap tidal cycle on shelf sea primary production. *J. Plankton Res.*, *30*, 183–197.
- Sharples, J., O. N. Ross, B. E. Scott, S. P. R. Greenstreet, and H. Fraser. 2006. Inter-annual variability in the timing of stratification and the spring bloom in the Northwestern North Sea. *Cont. Shelf Res.*, *26*, 733–751.
- Sharples, J., J. F. Tweddle, J. A. M. Green, M. R. Palmer, Y.-N. Kim, A. E. Hickman, P. M. Holligan, C. M. Moore, T. P. Rippeth, J. H. Simpson, and V. Krivtsov. 2007. Spring-neap modulation of internal tide mixing and vertical nitrate fluxes at a shelf edge in summer. *Limnol. Oceanogr.*, *52*, 1735–1747.
- Simpson, J. H. 1981. The shelf-sea fronts: implications of their existence and behaviour. *Phil. Trans. R. Soc. Lond. A*, *302*, 531–546.
- 1988. Tidal processes in shelf seas, in *The Sea*, *10*, K. H. Brink and A. R. Robinson, eds., John Wiley.
- Simpson, J. H. and J. R. Hunter. 1974. Fronts in the Irish Sea. *Nature*, *250*, 404–406.
- Simpson, J. H. and J. D. James. 1986. Coastal and estuarine fronts, in *Baroclinic Processes of Continental Shelves, Coastal and Estuarine Sciences*, C. N. K. Mooers, ed., *3*, Am. Geophys. Union, Washington, DC.
- Simpson, J. H. and J. Sharples. 1994. Does the earth's rotation influence the position of the shelf sea fronts? *J. Geophys. Res.*, *99*, 3315–3319.
- Speer, K. 1997. A note on average cross-isopycnal mixing in the North Atlantic Ocean. *Deep-Sea Res. I*, *44*, 1981–1990.
- Speer, K. G. and E. Tziperman. 1992. Rates of water mass formation in the North Atlantic Ocean. *J. Phys. Oceanogr.*, *22*, 93–104.
- Speer, K. G., H.-J. Isemer, and A. Biastoch. 1995. Global water mass formation from revised COADS data. *J. Phys. Oceanogr.*, *25*, 2444–2457.
- Thomas, H., Y. Bozec, K. Elkalay, and H. J. W. de Baar. 2004. Enhanced open ocean storage of CO₂ from shelf sea pumping. *Science*, *304*, 1005–1008.
- Walsh, G. 1982. On the relation between sea-surface heat flow and thermal circulation in the ocean. *Tellus*, *34*, 187–195.

Received: 24 May, 2010; revised: 20 September, 2010.